The International Journal of Advanced Manufacturing Technology (2021) 114:3615–3626
https://doi.org/10.1007/s00170-021-07038-x

ORIGINAL ARTICLE

Fabrication of monolithic SU-8 microneedle arrays having different needle geometries using a simplified process

Ajay A P[1,2] · Amitava DasGupta[2] · Dhiman Chatterjee[1]

Received: 28 August 2020 / Accepted: 1 April 2021 / Published online: 28 April 2021

Abstract

Transdermal drug delivery using hollow microneedle enables creating small, wearable and minimally invasive closed-loop system. Polymer hollow microneedles are preferable because they are cost-effective and easy to manufacture. SU-8 is chosen for creating the hollow microneedles as it is a biocompatible photopolymer with robust mechanical properties. Previously reported SU-8 microneedles either use melt casting process for coating SU-8 which is laborious or do not have monolithic structures, thereby making these mechanically weak and difficult to integrate. To the best of our knowledge, for the first time, we report the use of a single-step spin coating process to achieve the desired thickness of SU-8 while using UV lithography to create a monolithic microneedle array. Three types of microneedles were fabricated with outer dimensions varying from 90 to 180 μm, and lumen dimensions ranging from 60 to 80 μm and needle height of 600 μm. These needles are fabricated in a 10×10 array with a platform thickness of 300 μm. Geometrical, mechanical and fluid flow characterisations are carried out for the fabricated arrays. We report the use of a non-destructive evaluation method to characterise the lumen of the fabricated microneedles. The fabricated needles are robust and offer low resistance to fluid flow. The triangular needles can withstand a bending load of 0.2 N and an axial load of 0.7 N. The needles with circular lumen offer least resistance to fluid flow of 0.2 Pa-min μL^{-1}.

Keywords Microfabrication · Drug delivery · Monolithic · SU-8 · Polymer hollow microneedle

1 Introduction

Many therapies require controlled release of drugs over an extended period or require a feedback control, where the amount of drug depends on the real-time effect it has on the system. Achieving the abovementioned is not possible by oral medication or with hypodermic needles. Transdermal drug delivery, which was developed to resolve these issues, involves releasing drugs through the skin and allowing it to be picked up by the capillaries in the dermis layer by diffusion [1]. One of the major obstacles in transdermal drug delivery is the stratum corneum, which is a layer of dead cells covering the dermis. The stratum corneum needs to be disrupted to ensure better diffusion of the drug. Of the many methods developed and reported for disrupting the stratum corneum, use of microneedle is the only method available for delivering liquid formulations and large molecules which otherwise will not diffuse into the dermis [2].

Hollow microneedles form a part of the third-generation transdermal drug delivery system. They assist in breaking the skin barrier, thereby allowing the drug to be delivered to the dermis efficiently. They cause low pain and tissue damage compared to other drug delivery systems. They are also capable of delivering large molecules like proteins, vaccines and targeted drugs [3]. Over the years, a lot of research has been conducted in producing microneedles as well as in optimising their geometry, shape, and spacing [4–7]. Some of the important parameters that dictate microneedle design are (i) biocompatibility, (ii) ability to penetrate the stratum corneum, (iii) cost and ease of fabrication, (iv) pain associated with needle insertion, (v) resistance to the flow of drugs and (vi) integrability with other components to create a drug delivery system [1]. In order to reduce the pain felt, it is important to ensure that the needles do not enter the dermis, which is rich with nerve cells. At the same time, they should effectively penetrate

✉ Ajay A P
ajayap@smail.iitm.ac.in

[1] Department of Mechanical Engineering, IIT Madras, Chennai 600036, India

[2] Department of Electrical Engineering, IIT Madras, Chennai 600036, India

the epidermis. Hence, the needle lengths should be between 500 μm and 1000 μm to reach the junction between the dermis and epidermis [8, 9] and the microneedles should be capable of penetrating to this depth without breaking. Further, the fabrication process should be easily scalable for mass production and to be cost-effective.

Different materials like metal, silicon, and polymers have been used to fabricate microneedles. While metals are proven to be biocompatible and have high mechanical strength, the fabrication processes like LIGA are complex, and there is a safety risk if the material were to break off in the skin [10] accidentally. Silicon is the most common semiconductor material which has a mature microfabrication ecosystem. Silicon microneedles of many different shapes and cross-sections have been reported. But microneedle fabrication using silicon involves expensive and very controlled processes. In recent times, polymers are gaining significance as the material of choice for microneedle fabrication. Organic and some inorganic polymers have been proven to be biocompatible. They also have good mechanical properties and are amenable to many different fabrication processes like moulding, light-curing and embossing which ensure low cost and high throughput [11]. Many polymers like polylactic acid (PLA) [12], polylactic-co-glycolic acid (PLGA) [12], polymethyl methacrylate (PMMA) [10], hyaluronic acid (HA) [13] and SU-8 [8] have been used for producing microneedles. Hence, in this work, polymer is chosen as the material for fabricating the microneedle array.

Different fabrication processes like injection moulding [14, 15], micro-moulding [16], LIGA [17] and photolithography [8] have been used successfully to fabricate hollow polymer microneedles. Different types of polymers can be used in injection moulding to create needle arrays within a short time. The injection moulding processes reported in literature for creating hollow microneedles either requires a 2-step process involving laser ablation to create the lumen opening [14] or moulds having high aspect ratio micro-features to create the lumen [18]. The requirement of two separate processes, the issue of mould durability due to the presence of high aspect ratio micro-sized features and complexity involved in maintaining polymer melt temperature in the mould makes process scaling a challenge. Micro-moulding process is a hybrid fabrication process combining moulding with photolithography and so far is used to create bevelled edges at the microneedle tips. It has been shown that flat tip needles can penetrate human skin successfully [19], and hence, bevelling would only increase process complexity. The LIGA process combines lithography, moulding and electroplating using the complex and rarely available X-ray lithography process and is mostly used to realise metal microstructures. On the other hand, photolithography-based manufacturing is better suited to achieve high aspect ratio microtube structures with higher throughput compared to other manufacturing methods. Among the different polymers used for creating microneedles, SU-8 is the best suited to fabricate microneedles using photolithography.

SU-8 is a negative photoresist that is very well suited for microneedle fabrication due to its photo-polymerisation property allowing the creation of different shapes easily by photolithography compared to other polymers. As it is already used extensively in the semiconductor industry, it can be integrated easily into standard microfabrication process lines. It has been proven to be biocompatible [20] and has good mechanical properties. Cured SU-8 is hydrophobic unlike other photopolymers like PMMA, which ensures that drugs like injectable insulin do not stick to the needles [21, 22].

Huang et al. [23] reported the development of microneedle arrays by ultra-violet (UV) lithography process. The patch had a platform made of polydimethylsiloxane (PDMS) to ensure that it is flexible. The fabrication process involved multiple lithographic steps and a simultaneous double mask exposure that makes the process complicated. The authors did not report any characterisation results of the patches. The reported height of the needles was less than 210 μm which, as discussed earlier, is not sufficient for reaching the junction between the dermis and epidermis. Ceyssens et al. [8] used a hybrid process combining micro-moulding and UV lithography to produce bevelled tip microneedles. They reported needles of circular and triangular cross-sections with heights of 800 μm integrated with a 200-μm thick platform of the same material in a monolithic structure. They used melt casting of SU-8, which is a laborious process, to achieve a film of desired thickness. Wang et al. [24, 25] improvised on this and developed a PDMS mould to create pyramidal and hypodermic type microneedles. They realised two designs of needle, both having heights of 1000 μm where one had a square cross-section with a width of 400 μm and a circular lumen while the other had a circular cross-section and a circular lumen with an outside diameter of 300 μm. However, it may be noted that the use of PDMS mould is affected by the expansion of the moulds during pre-bake and also involves an elaborate process to produce the inclined walls of the PDMS mould. Thanh et al. [26] produced microneedles of different heights and a cross-section of 300 μm width using a CNC micromachined aluminium mould. The large widths of the needles they fabricated may lead to pain during insertion. More recently, Mishra et al. [27] presented a direct laser writing-based fabrication method to produce microneedles having a height of 500 μm on a silicon platform with pre-formed vias for fluidic interconnection. They used a non-bevelled needle design as the calculated skin penetration forces were reported to be well below the compressive failure load of the designed needles and thereby reducing process complexity. The process has some drawbacks like elaborate and complex alignment procedure to create the vias in silicon, long writing times involved in direct laser writing and hence low throughput compared to UV

lithography, low failure load in bending as it is limited by the adhesion force between SU-8 and silicon.

The commonly used method to achieve a 1-mm thick SU-8 layer, as mentioned above, is the melt casting method. This method increases the process complexity. Microneedle arrays having a monolithic structure, where the needles are integrated with a platform of the same material, have better mechanical strength and enable fluid interconnection with other components in a drug delivery system [8, 24, 25]. In this paper, the use of a single-step spin coating process, to achieve the desired thickness of ~ 1mm SU-8 needed to create a monolithic microneedle array, is reported for the first time. We present the fabrication and characterisation of a monolithic SU-8 microneedle array with a platform providing fluid interconnection with other systems. An oxide layer has been introduced on the substrate to reduce damage to needle tips. Three microneedle geometries are evaluated in terms of their suitability for drug delivery applications. We report the use of a non-destructive evaluation technique to visualise and characterise the fabricated needle lumen. To the best of our knowledge, these developments have not been reported in literature.

In Section 2, we present the needle geometries and an outline of the fabrication procedure. In Section 3, we present the results of fabrication and characterisation of the fabricated needles.

2 Methodology

2.1 Design

Three cross-sectional profiles of the microneedle shown in Fig. 1 are considered in this work. Figure 1a shows a circular needle of diameter d_o with a circular lumen of diameter d_i. Figure 1b shows a triangular needle of base h_o with a triangular lumen of base h_i. Figure 1c shows a triangular needle of base h_o with a circular lumen of diameter d_i. The triangles are isosceles having a height equal to the base.

The pain felt during needle insertion increases with increase in the size of the needle, while the mechanical strength of a microneedle depends on the size of its base [7, 28]. Diffraction of light from the lithographic patterns causes tapering of the needle profile. Hence, the dimensions shown in Table 1 are chosen keeping in mind the limitations of the fabrication process and mechanical stability of the fabricated needle. A needle height of 600 μm was chosen to target the junction between the dermis and epidermis. The wall thickness is kept at 15 μm as it is the minimum wall thickness required to prevent the failure of needles by buckling under axial load [9]. In the case of the triangular needle with a circular lumen, the lumen is centred at the incentre of the triangle, and the minimum wall thickness is kept at 15 μm. The design with a circular needle and a circular lumen is one of the most commonly reported microneedle geometries. Hence, this design was chosen to compare the characteristics of the microneedles produced by the present method with those produced by other methods. The design with a triangular needle and triangular lumen was chosen to compare the mechanical strength of the microneedles produced by the proposed fabrication process with those in literature [8]. The design with a triangular needle and a circular lumen was chosen as the increased annular area is expected to enhance the structural stability of the needle.

2.2 Fabrication

The fabricated array consists of 100 needles in a 10×10 pattern. These are connected to a platform of the same material having a thickness of 300 μm, thereby producing a monolithic structure. The patch dimensions are 8.5 mm × 8.5 mm with the array at the centre.

The fabrication process involves the use of conventional UV lithography with two masks, as shown schematically in Fig. 2. SU-8 2150 is used to create the needles. It is a negative photoresist and is commonly used to fabricate high aspect ratio structures in the microelectronics industry. The process starts with a cleaning of the silicon substrate. A p-type <100> silicon wafer is diced into 3 cm × 4 cm pieces. The pieces are cleaned by washing in boiling acetone and then with isopropyl alcohol (IPA). After blow-drying the samples with nitrogen, they are subjected to cleaning with piranha solution (3:1, H_2SO_4:H_2O_2) for 5 min to remove any organic residues and oxidise the surface. Following this, the pieces are placed in

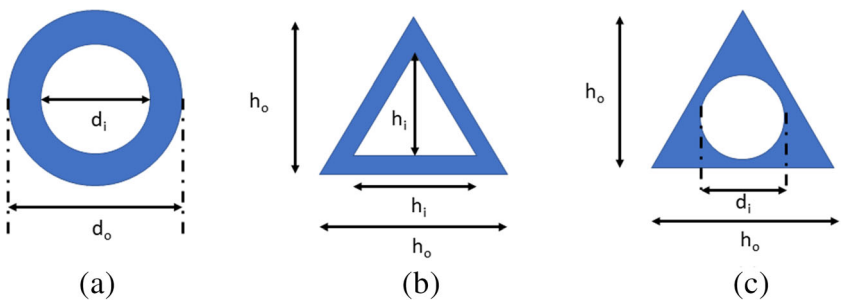

Fig 1 Cross-sectional profiles of the microneedles. (**a**) Circular needle body and circular lumen (Design 1), (**b**) triangular needle body and triangular lumen (Design 2) and (**c**) triangular needle body and circular lumen (Design 3)

Table 1 Microneedle dimension

Reference	Design No	Dimension (μm)
Figure 1 a	1a	d_i=60; d_o=90
	1b	d_i=80; d_o=110
Figure 1 b	2a	h_i=80; h_o=130
	2b	h_i=90; h_o=140
Figure 1 c	3a	d_i=60; h_o=146
	3b	d_i=80; h_o=178

fuming HNO_3 for 2 min. This process creates a thin oxide layer on the silicon surface. They are then washed in de-ionised (DI) water and blow-dried (Fig 2a). The thin oxide layer helps in reducing the adhesion between SU-8 and the substrate [29].

The substrate is then placed on a weighing balance, and 0.3 g cm^{-2} of SU-8 2150 is poured on it. The samples are then allowed to rest on a flat surface for 2 min to allow the SU-8 to spread under its weight. Then it is placed in a spin coater and spun, first at 200 rpm for 15 s and then at 400 rpm for 45 s at an acceleration of 300 rpm s^{-1}. These parameters have been optimised to achieve a SU-8 film thickness of 900 ± 100 μm (Fig. 2b). A single-step spin coating process achieves the SU-8 film as against the melt casting method reported by [8]. This reduces the process complexity while retaining the properties of the resist.

After allowing the spin-coated substrate to rest for some time, it is subjected to pre-bake to reduce the solvent concentration. This ensures good pattern reproducibility by reducing photo-acid diffusion and also ensures that the resist does not stick to the mask during UV exposure. The pre-bake is carried out on a level hot plate during which the temperature is raised from room temperature to 110 °C gradually over 5 h. The samples are held at 110 °C for 7.5 h and then gradually brought down to room temperature over 6 h. The gradual ramping up and down of temperature ensures that there are minimal residual stresses in the SU-8 film.

Now the sample is subjected to UV exposure to realise the needle body with the lumen (Fig. 2c). UV light of 405 nm (Karl Suss MA6/BA6 aligner) is used. A 5-mm PMMA filter is used to filter light below 400 nm in the first exposure. The absorption coefficient of SU-8 at 405 nm is lower than that at 365 nm, allowing the light to reach and cure regions at the bottom of the SU-8 film. The exposure energy is 13,500 mJ cm^{-2}, which is optimised over several trials. The exposure is carried out over 34 cycles, with each cycle having an exposure energy of 400 mJ cm^{-2} with a 30-s wait time between cycles. This helps in avoiding the resist from heating up and reducing photo-acid diffusion [30]. In the second UV exposure, a different mask that covers the lumen area is used. Significant misalignment compensation is provided in the mask design itself. UV light of 365 nm is used to create the platform which holds the needles. Due to the high absorption coefficient of SU-8 at 365 nm, the top few hundred microns of the SU-8 layer is exposed by controlling the exposure energy (Fig. 2d). The top layer thus formed creates a monolithic structure without the need for a platform of a different material for providing a fluidic connection to the drug reservoir or a micropump. The exposure energy used is 75 mJ cm^{-2} which is optimised to achieve a 300-μm thick platform.

The sample is then subjected to a post-exposure bake. Here again, the substrate is kept on a hotplate and gradually heated from room temperature to 60 °C over 40 min. The sample is held at 60 °C for 5 min and gradually cooled to room temperature over 1 h. It is followed by development in the SU-8 developer solution (Fig. 2e). Ultrasonication is used to speed up the development process. Once the individual patches separate from the substrate, they are again ultrasonicated in the developer for 2 min to aid better development of the lumens. They are then rinsed in IPA and blow-dried with a low-pressure stream of nitrogen (Fig. 2f).

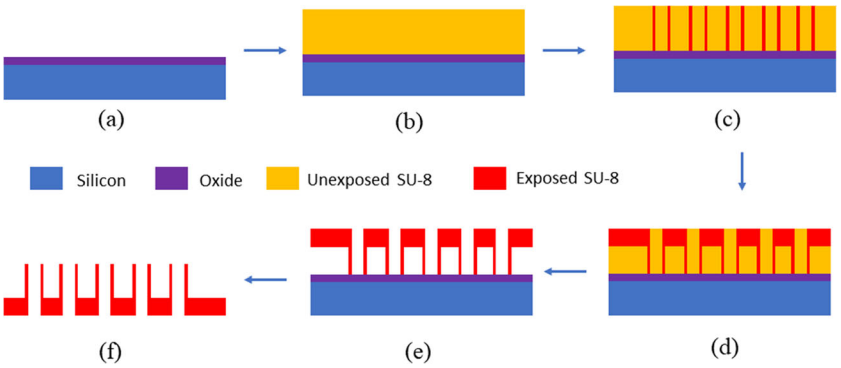

Fig 2 Steps involved in the fabrication of microneedle array (**a**) silicon substrate with a thin oxide layer, (**b**) 1mm SU-8 spin coated and pre-baked, (**c**) needle body and lumen created in SU-8 after 1st UV exposure (**d**) 300 μm platform with holes aligned to needle lumen, created in SU-8 by a dose-controlled 2nd UV exposure, (**e**) structure after post exposure bake and development and (**f**) final microneedle patch separated from the substrate

3 Results and discussion

3.1 Geometric characterisation

The fabricated microneedles are imaged using confocal microscopy (Olympus LEXT OLS4000) and scanning electron microscopy (SEC SNE4500M). For SEM, the samples are gold coated on a tabletop sputter coater, and a scan voltage of 30 kV is used for imaging. The openings at both ends of the needles along with the height and outer needle dimensions are measured. The platform thickness is measured using a digital micrometer. An X-ray computational tomography (CT) analysis is performed (GE Sensing phoenix v|tome|x s) on the gold-coated microneedle patches to characterise the inner lumen profile. An X-ray tube voltage of 40 kV and a current of 120 μA are used. The X-ray exposure is set at 68 ms, and a total of 2000 images are taken to construct the tomogram. The voxel size is 5.3 μm

Several microneedle patches of each proposed design are fabricated, and the process is found to be repeatable. The SEM images, some of which are shown in Fig. 3, show needles with through lumens having a height of 600 ± 50 μm and a platform thickness of 300 ± 20 μm. A minimum of five arrays of each design are used for measurements with 2 needles per array being measured. Table 2 shows the mean and deviation of these measurements along with the variation between the designed and achieved dimensions of the needles for all designs considered. As the light bends due to diffraction in UV lithography, a reduction in the lumen dimension from the design value is observed as shown in Table 2. The use of 405-nm light and the reduced photo-acid diffusion due to multi-step exposure reduces tapering of the needle profile. This allows achieving lumens with diameters as small as 40 μm. The use of SiO_2 layer on the silicon substrate helps to reduce the tip surface damage by reducing adhesion of patches to the substrate.

Designs 1a, 2a and 2b showed low fabrication yield. SU-8 is observed to be highly pliable immediately after development. This tends to cause some needles in the array of design 1a (cylindrical needle and circular lumen) to bend as they are mechanically weak owing to the small base diameter and stick to adjacent needles thereby reducing the number of usable arrays of this design. The needles with triangular lumen show a higher reduction in lumen dimension with the lumen being completely blocked in some cases compared to the circular lumen due to rounding of the sharp triangular corners.

Needles with triangular bodies are straight owing to the stability of their design. No alignment issues are observed as the mask design allows for significant misalignment and sharp latent image of the alignment marks formed in the resist after the first UV exposure assisted in the second alignment step. From a geometric perspective, it is found that triangular needles with circular lumens are closer to the designed dimensions.

Though Ref. [31] has used X-ray micro-CT to study the flow passage on the outer surface of a microneedle, to the best of our knowledge, it is for the first time that X-ray micro-CT is used to study the lumen in the microneedles in order to detect the presence of any blockage due to either debris or tapering owing to the fabrication method. Figure 4 shows the cross-sectional profiles and 3-D reconstructed images of the microneedle array of each design. The images show that the lumens have been formed throughout the length of the needles. It is also observed that the tapering of the lumen begins at the point where the needles emerge from the platform. From the cross-sectional profile, it can be concluded that the fabrication process is capable of producing needles having a lumen throughout the length of the needle.

3.2 Mechanical characterisation

The patches are subjected to compression tests (load applied perpendicular to needle patch) using an Instron Micro Tensile Tester (Instron UTS 5948). This test gives the maximum axial load the microneedle can withstand. One patch of each design is stuck to an in-house designed acrylic fixture with a scotch tape. A plunger is pressed against the needles at 0.08 mm min^{-1}. A micro-force sensor measures the reaction force as the plunger moves. The needles are deemed to have failed when there is a sudden drop in the force measured.

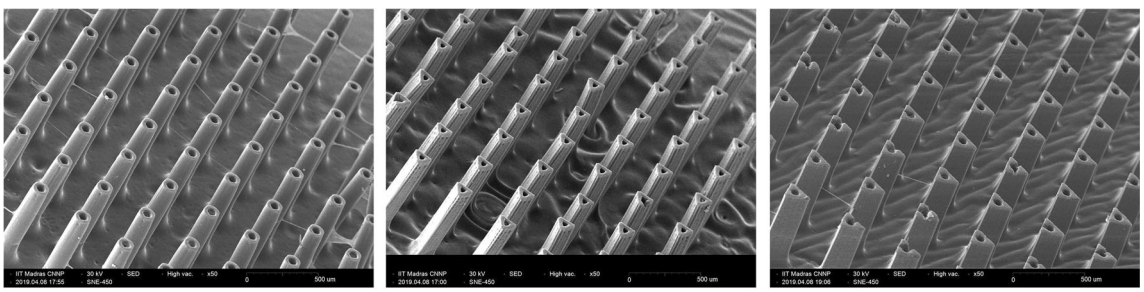

(a) (b) (c)

Fig. 3 SEM images of microneedle arrays with (**a**) cylindrical needle and circular lumen, (**b**) triangular needle and triangular lumen and (**c**) triangular needle and circular lumen

Table 2 Comparison of microneedle dimensions achieved with the designed values

Design no.	Parameter name	Designed value (μm)	Achieved dimension (μm)	DIFFERENCE (μm)
1a	d_i	60	37.3 ± 5	22.7
	d_o	90	85.7 ± 15	4.3
1b	d_i	80	58.3 ± 8	21.7
	d_o	110	104.4 ± 10	5.6
2a	h_i	80	45.4 ± 5	34.6
	h_o	130	117 ± 7	13
2b	h_i	90	55.6 ± 10	34.4
	h_o	140	128 ± 5	12
3a	d_i	60	46 ± 8	14
	h_o	146	133 ± 7	13
3b	d_i	80	63.7 ± 9	16.3
	h_o	178	162.1 ± 10	15.9

Next, another set of patches, one of each design, are subjected to bending test using the same Instron tester and the acrylic fixture. The patches are prepared such that each patch has only one row of microneedles. The jig used for the bending moment experiments is designed such that the plunger is offset from the jig face by 600 μm (Fig. 5a). Hence, for all the microneedles, the point of contact of the plunger and the needle should be about 300 μm from the base of the needle as the thickness of the needle patch is 300 ± 20 μm. This ensures that the point of bending load application is almost the same for all the needles. A plunger moves perpendicular to the needle axis at 0.08 mm min^{-1} and bends one needle at a time until it breaks. This test gives the maximum bending load that the needles can withstand.

Figure 6 shows the representative graphs of force versus displacement values obtained from compression and bending tests. The point in the graph of force versus displacement at which there is a sudden drop in the force is considered the force at failure. In the case of compression, the value of the force obtained is divided by the number of needles to get the maximum compressive force per needle. It may be noted that the dimension of the plunger surface contacting the array is 5 mm × 30 mm, whereas the maximum area occupied by the microneedles in the array is 3.9 mm × 3.9 mm. Hence, the contacting surface is larger than the area of the needle array. Also, the total vertical traverse of the plunger, before needle failure occurs, is around 200 μm which is greater than the maximum height deviation of 50 μm recorded among the needles in an array. Hence, we can conclude that the plunger will contact all the needles before the point of failure. Experiments were repeated three times, and the results show the variation of failure loads obtained from different

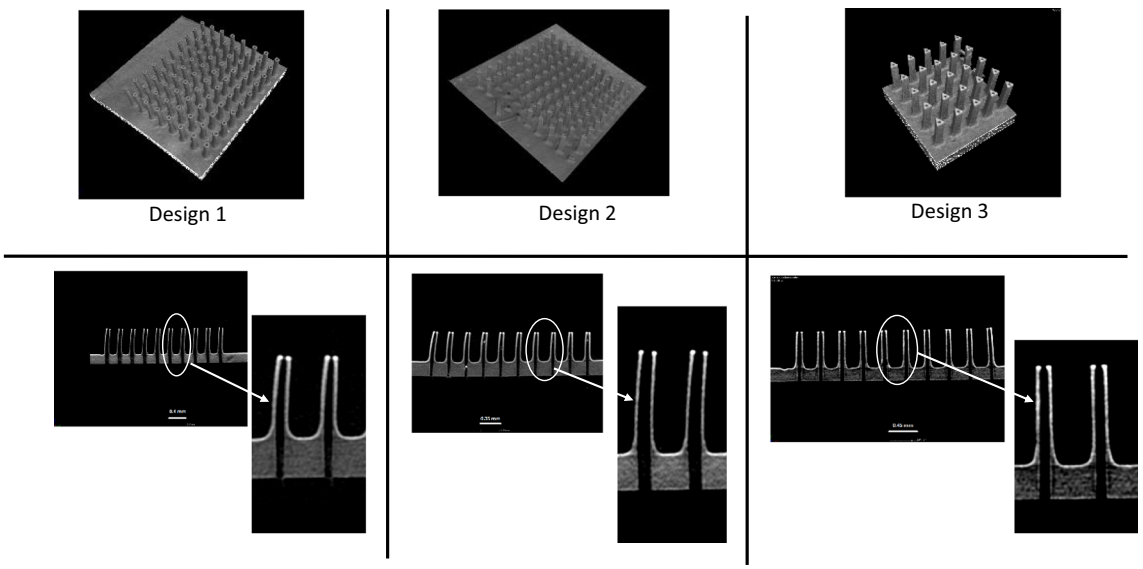

Fig. 4 (Top) 3-D reconstructed images from the CT scan. (Bottom) Cross-sectional X-ray CT images of the microneedles

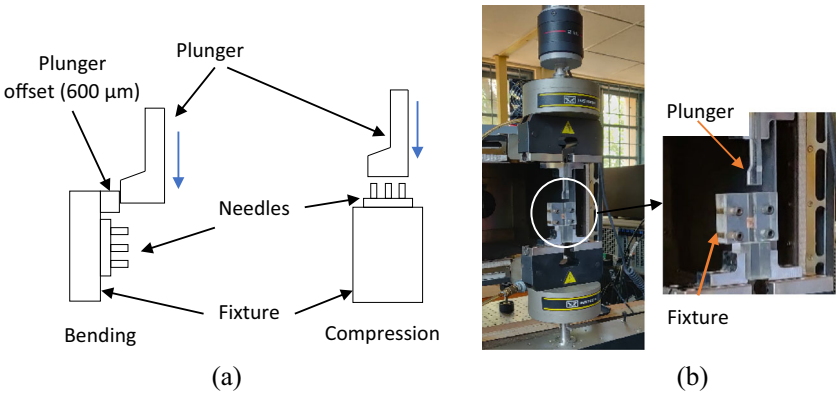

Fig. 5 (**a**) Schematic showing method of loading in bending and compression. (**b**) A photograph of the setup and the acrylic fixture used for mechanical characterisation arranged in the bending test configuration

experiments in the form of error bars. The error bars indicate that the results are reasonably well-repeated. Hence, even though there is no way to quantitatively know the exact number of needles in contact at the same value of compression, we do not expect the number of needles compressed to be very different from each other in each of these tests. To better understand the effect of compression test on a single needle rather than an array, a few tests were carried out for Design 3b and this is reported later.

Figure 7 shows the variation of axial load and bending loads at failure. It is clear that needles having circular external geometry (Design 1) fail at a lower value of load, in comparison to that of triangular exterior (Designs 2 and 3). In particular, Design 3b shows the best performance under both loading conditions. Before we explain the possible reasons behind these observations, we present a comparison of the compressive load at failure of Design 3b as an array, and as a single microneedle. As opposed to the compressive load in the range of 0.6–0.85 N for an array of Design 3b (when expressed as failure load per unit microneedle), single microneedle was found to fail in the range of 1.2–1.3 N. These values are slightly higher than the corresponding values for an array, thereby possibly indicating that dividing the total compressive force by the total number of microneedles is a conservative estimate. However, as shown later, even this conservative estimate is higher than the skin penetration force required.

We now analyse the data presented in Fig. 7 more closely. When subjected to a compressive load, the mechanical response of the needles can be treated as columns of different slenderness ratio (L/r) and area moments of inertia. Table 3 gives these quantities for different designs used in the present work. For SU-8, based on stress at proportional limit considered as 60 MPa and Young's modulus of 2 GPa (from SU-8 2150 material datasheet), the critical value of slenderness ratio [32] above which columns can be considered long column is estimated as 9.07. Hence, all the microneedles under consideration here are expected to show buckling if the load exceeds the critical load for buckling. The critical values of loads for onset of buckling are given in Table 3. The loads at which the failures take place are, however, much higher than the critical compressive load needed to induce buckling, thereby indicating that the failure occurs because of compression and buckling instability. The same figure also shows that the transverse loading or bending loads at failure are much lower. This is because of the possibility of existence of large bending moment at the base of the microneedles due to their long lengths. However, as shown in Fig. 7, the forces at failure due to axial or bending loading for each of the arrays are much larger than

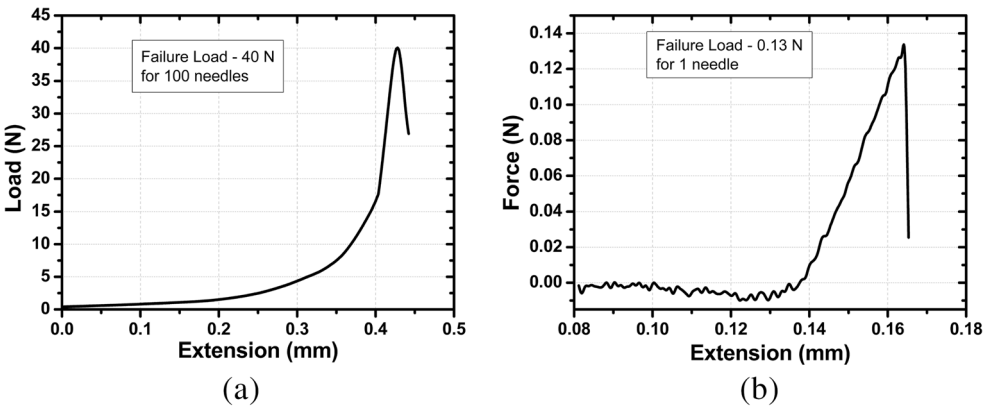

Fig. 6 Typical load vs extension graph showing failure load in (**a**) compression and (**b**) bending for design number 2a

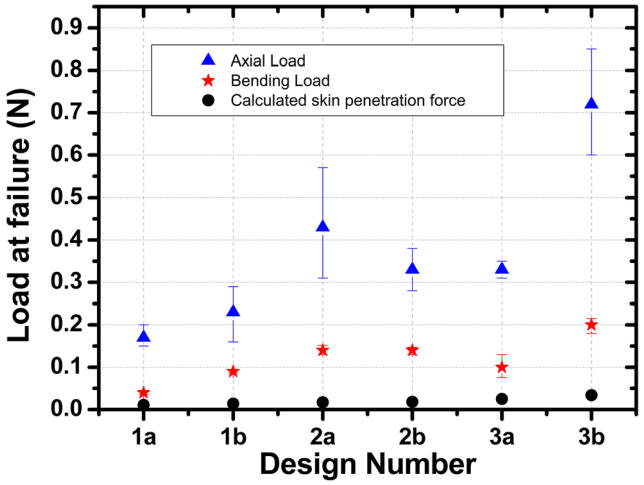

Fig. 7 Failure loads due to compressive (axial) and bending estimated for each microneedle in an array. Also shown in the same figure are the estimated skin penetration forces

the skin penetration force. Skin penetration force can be estimated from the knowledge of the puncture pressure and respective needle areas. From literature, it is known that the puncture pressure required to penetrate the skin is about 3.18 MPa [33]. By multiplying this value with the area at the respective needle tip, skin penetration forces for each design can be estimated and are shown in Fig. 7. Thus, from the tests on an array as well as limited experiments on a single needle, it is evident that the needles fabricated using the present method not only have failure loads well above the estimated skin penetration force but also the critical load for buckling for each design is above the skin penetration force. These polymeric microneedles will not even buckle during insertion into the skin and hence are safe to use as needles for drug delivery.

The failure modes become qualitatively apparent from the SEM images of microneedles taken after compressive and bending loads. For the purpose of illustrating these effects qualitatively, Fig. 8 presents SEM images of Designs 1a and 2a. Design 1a which has about 2.6 times lower moment of inertia compared to Design 1b not only fails early, as shown in Fig. 7, but also fails at a much higher height from the base in comparison to Design 2a. These SEM images, therefore, qualitatively portray that buckling plays a more important role in Design 1a than in Design 2a. A comparison of locations of failure under compressive and bending loads indicates that the height at which failure occurs due to bending is closer to the base in comparison to that due to compression. This is expected as the highest bending moment typically occurs at the base.

It is also important to compare the failure loads obtained in the present work with that available in the literature. Compared to the failure load of 0.23 N for needles produced using the melt casting method [8], the needles of similar shape produced by the presented method show a failure load of 0.33 N. The difference can be attributed to an increase in the final wall thickness achieved in our case. Thus, it shows that the present method can produce needles having similar or better mechanical characteristics as those reported in the literature but using a simpler fabrication method. Compared to the microneedles produced by [27], where the needles and the platform are made of different materials and show a bending load at failure of around 0.022 N, the bending load at failure in the case of our needles having a monolithic structure is observed to be an order of magnitude higher. Hence, the monolithic structure improves the bending load at failure of the microneedles. From the point of mechanical strength of the needles, triangular needles show higher failure loads in both bending and compression compared to cylindrical needles.

3.3 Fluid flow characterisation

Patches of Design 1a are found to be mechanically weak with severe bending of needles being observed after development, and have lower fabrication yield. Hence, only patches of designs other than 1a are subjected to fluid flow analysis. The needle patches are tested individually to measure the

Table 3 Geometric properties of microneedles treated as columns

Design no.	Length of microneedles used for compression testing based on confocal microscopy, L (μm)	Area moment of inertia $\times 10^{-6}$ (μm^4)	Cross–sectional area (μm^2)	Radius of gyration, r (μm)	Slenderness ratio, L/r, of microneedles used for compression testing	Critical load for buckling using Euler's column formula (N)
1a	505.20	2.584	4247.34	27.04	18.68	0.04
1b	606.36	5.176	5145.31	34.00	17.83	0.09
2a	561.20	6.781	5684.00	35.94	15.61	0.09
2b	608.23	8.829	5545.19	39.19	15.52	0.08
3a	582.85	11.934	6298.25	39.04	14.93	0.13
3b	584.60	25.737	9814.41	48.78	11.98	0.27

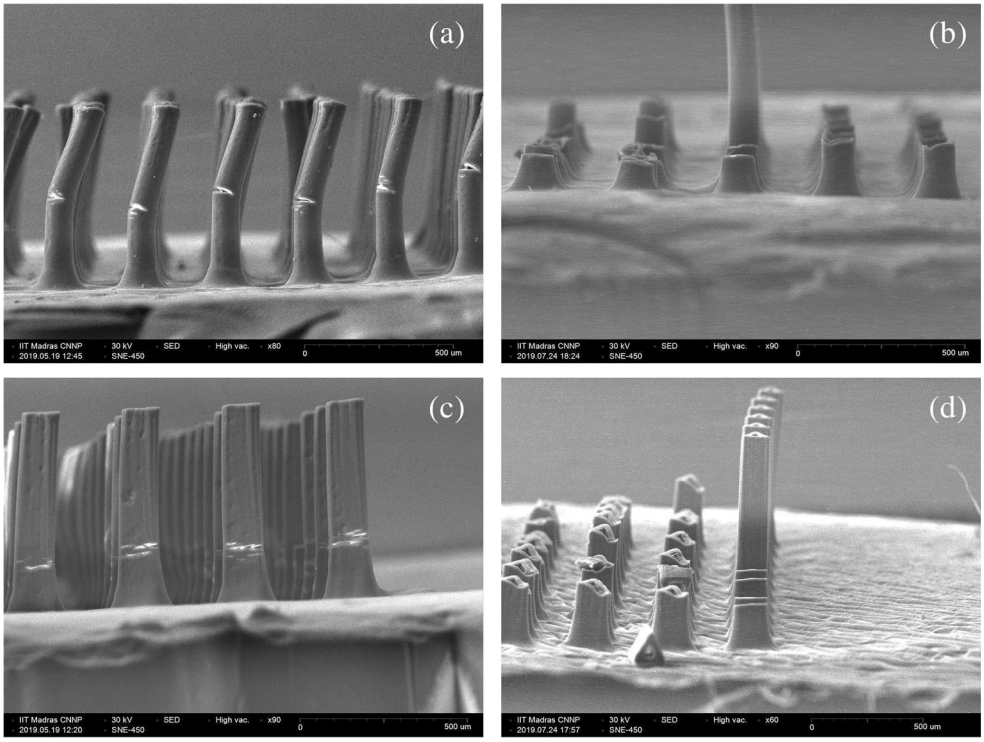

Fig. 8 SEM images of Design 1a (photographs **a** and **b**) and Design 2a (photographs **c** and **d**) after compression test (**a** and **c**) and bending (**b** and **d**). The circled area shows location of failure

resistance offered by the microneedles to fluid flow. An acrylic fixture is designed and fabricated to carry out fluid flow experiments. Figure 9a shows a schematic with different components of the experimental setup. The fixture along with the needle patch is connected to a syringe pump (New Era Pumping system, NE-1000) and a differential pressure transducer (Omega PX26-005DV) as shown in Fig. 9b. Water is flown at a high rate in order to observe a jet of water released from the needles as shown in Fig. 9c indicating that the needle lumens are not blocked. Next, the syringe pump drives the flow at preset flowrates and the differential pressure transducer measures the pressure at the inlet of the fixture. A graph of flowrate vs pressure is plotted, and the slope of this graph gives the resistance offered by the needle for the flow. Figure 10a shows the variation of pressure at different flow rates for Designs 2a and 3a, and Fig. 10b shows the same for Designs 1b, 2b, and 3b.

It is observed that the fluid flow resistance, which is given by the slope of the variation in pressure with flowrate in Fig. 10, increases with a decrease in the lumen size, and a triangular lumen offers higher resistance to flow than a circular lumen having similar hydraulic diameters. Table 4 shows the resistance values calculated from experiments. This resistance is inversely proportional to the number of needles and hence,

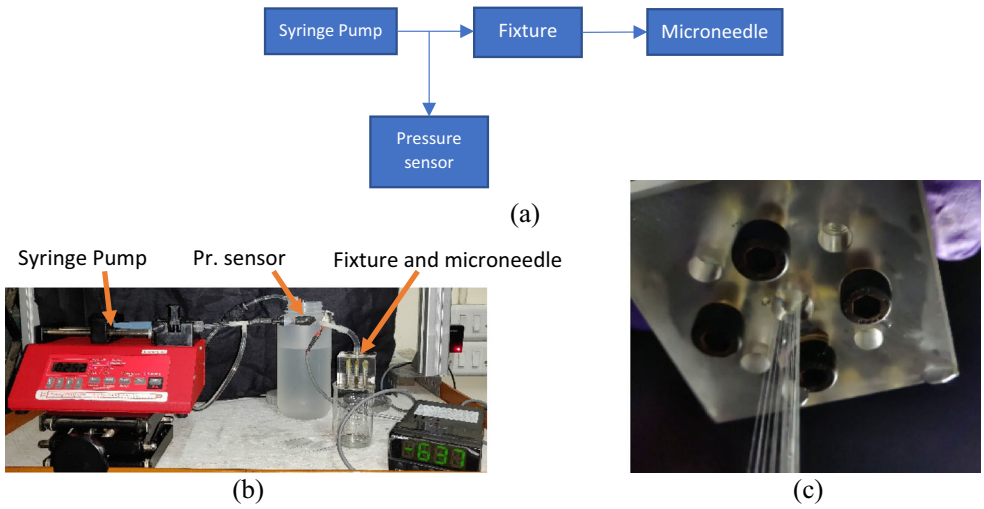

Fig 9 (**a**) Schematic of the fluid flow characterisation, (**b**) photograph of the test setup and (**c**) water streaming from the needle array when flown at high rate

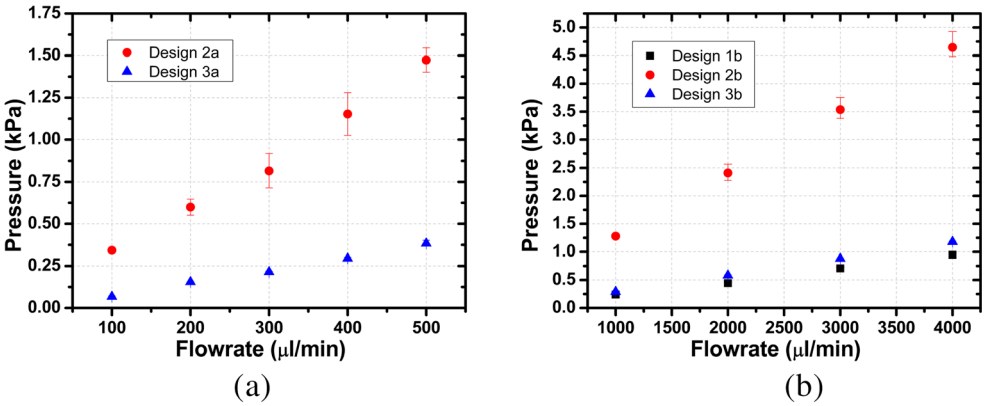

Fig. 10 (**a**) Pressure vs flowrate graph for designs 2a and 3a (**b**) for designs 1b, 2b and 3b

when arranged in an array, provide minimal resistance to flow (at the flowrates of 3–4 μL min^{-1} typically used for drug delivery) compared to that offered by the skin which is around 44 Pa-min μL^{-1} [34].

For a circular channel with diameter d, the fluid flow resistance can be calculated from the Hagen-Poisuelle equation as:

$$Resistance = \frac{128\mu L}{\pi d^4} \quad (1)$$

Where μ is the viscosity of liquid, L is the channel length (which is the sum of needle height and patch thickness in this case). The resistance calculated in this way for Design 3b is 27.86 Pa-min μL^{-1} which is in close agreement with the experimentally obtained resistance of 26.1 Pa-min μL^{-1}. From the resistance values shown in Table 4, we can see that triangular lumen offers higher resistance than circular lumen having a diameter equal to the height of the triangle. This is due to the hydraulic diameter of the triangular lumen being smaller than the circular lumen. Hence, from a fluid flow perspective, circular lumen is found to be better than the triangular lumen.

4 Conclusion

In the present work, a single-step spin coating method is used for preparing SU-8 layers, which are used to fabricate monolithic hollow microneedle arrays along with patches using UV lithography. Using our fabrication process, which is repeatable and reliable, a large number of patches with needle arrays can be produced simultaneously, thus facilitating mass production. Three different cross-sectional profiles with either circular or triangular-shaped body and lumen were chosen for study. A non-destructive testing method, which is used to inspect the needle lumen, along with fluid flow experiments shows that the fabricated needles have clearly defined lumens. The results from compression and bending tests show that the fabricated needles are mechanically robust with failure loads much higher than the skin penetration force. Hence, the hollow microneedles presented in this work are capable of penetrating skin without failure. The monolithic structure of patch and microneedle array in our work is probably the reason for higher bending strength of the needles compared to results reported earlier. The triangular needle design is able to withstand a bending load of 0.2 N and an axial load of 0.72 N. In terms of mechanical strength, the triangular needles show higher failure forces compared to the cylindrical needles. The triangular needles with circular lumens have the least deviation from designed dimensions while having higher mechanical stability. The needles with cylindrical lumens provide lower resistance to fluid flow than those with triangular lumens. Hence, we conclude that a triangular needle with a circular lumen is the optimal needle profile among those considered, in terms of mechanical stability and fluid flow resistance.

Table 4 Fluid flow resistance

Design no.	Achieved lumen hydraulic dia (μm)	Experimental fluid flow resistance (Pa-min μL^{-1})
1b	59.5	24
2a	28.8	170.4
2b	34.7	89.6
3a	50.1	77
3b	65.6	26.1

Acknowledgements The fabrication was carried out at the Centre for NEMS and Nano Photonics (CNNP) (sponsored by MeitY and DST, Govt. of India). The authors would like to acknowledge Dr. Amitava Ghosh for help with fabricating the testing jigs, Dr. Sushanth K Panigrahi for the use of micro tensile tester (DST-FIST SR/FST/ETI-059/2013) and Mr. Gopalakrishnan for the assistance provided in conducting the mechanical characterisations. The authors wish to acknowledge Centre for Non Destructive Evaluation (CNDE) for allowing the use of their micro-CT facility. The authors would also like to thank the technical staff, MEMS and Microelectronics Laboratory, IIT Madras for their support.

Author contribution Attiguppe P Ajay was involved in conceptualisation and investigation of the current study. Amitava DasGupta and Dhiman

Chatterjee supervised the work and provided extensive advice during the design of the needles and experimental analysis. They also extensively reviewed and edited the manuscript.

Availability of data and materials Not applicable.

Declarations

Ethical approval Not applicable.

Consent to publish The authors provide their consent for the above article to be published in the International Journal of Advanced Manufacturing Technology.

Conflict of interest The authors declare no competing interests.

References

1. Henry S, McAllister DV, Allen MG, Prausnitz MR (1998) Microfabricated microneedles: a novel approach to transdermal drug delivery. J Pharm Sci 87:922–925. https://doi.org/10.1021/js980042+
2. Prausnitz MR, Langer R (2008) Transdermal drug delivery. Nat Biotechnol 26:1261–1268. https://doi.org/10.1038/nbt.1504
3. Giri Nandagopal MS, Antony R, Rangabhashiyam S, Sreekumar N, Selvaraju N (2014) Overview of microneedle system: a third generation transdermal drug delivery approach. Microsyst Technol 20:1249–1272. https://doi.org/10.1007/s00542-014-2233-5
4. Al-Qallaf B, Das DB (2009) Optimizing microneedle arrays for transdermal drug delivery: extension to non-square distribution of microneedles. J Drug Target 17:108–122. https://doi.org/10.1080/10611860802472370
5. Olatunji O, Das DB, Garland MJ, Belaid L, Donnelly RF (2013) Influence of array interspacing on the force required for successful microneedle skin penetration: theoretical and practical approaches. J Pharm Sci 102:1209–1221. https://doi.org/10.1002/jps.23439
6. Bal SM, Kruithof AC, Zwier R, Dietz E, Bouwstra JA, Lademann J, Meinke MC (2010) Influence of microneedle shape on the transport of a fluorescent dye into human skin in vivo. J Control Release 147:218–224. https://doi.org/10.1016/j.jconrel.2010.07.104
7. Kochhar JS, Quek TC, Soon WJ, Choi J, Zou S, Kang L (2013) Effect of microneedle geometry and supporting substrate on microneedle array penetration into skin. J Pharm Sci 102:4100–4108. https://doi.org/10.1002/jps.23724
8. Ceyssens F, Chaudhri BP, Van Hoof C, Puers R (2013) Fabrication process for tall, sharp, hollow, high aspect ratio polymer microneedles on a platform. J Micromech Microeng 23:075023. https://doi.org/10.1088/0960-1317/23/7/075023
9. Chaudhri BP, Ceyssens F, De Moor P et al (2010) A high aspect ratio SU-8 fabrication technique for hollow microneedles for transdermal drug delivery and blood extraction. J Micromech Microeng 20:064006. https://doi.org/10.1088/0960-1317/20/6/064006
10. Jin CY, Han MH, Lee SS, Choi YH (2009) Mass producible and biocompatible microneedle patch and functional verification of its usefulness for transdermal drug delivery. Biomed Microdevices 11:1195–1203. https://doi.org/10.1007/s10544-009-9337-1
11. Sullivan SP (2009) Polymer microneedles for transdermal delivery of biopharmaceuticals. Georgia Institute of Technology
12. Park JH, Allen MG, Prausnitz MR (2005) Biodegradable polymer microneedles: fabrication, mechanics and transdermal drug delivery. J Control Release 104:51–66. https://doi.org/10.1016/j.jconrel.2005.02.002
13. Liu S, Jin MN, Quan YS, Kamiyama F, Katsumi H, Sakane T, Yamamoto A (2012) The development and characteristics of novel microneedle arrays fabricated from hyaluronic acid, and their application in the transdermal delivery of insulin. J Control Release 161:933–941. https://doi.org/10.1016/j.jconrel.2012.05.030
14. Lhernould MS, Deleers M, Delchambre A (2015) Hollow polymer microneedles array resistance and insertion tests. Int J Pharm 480:152–157. https://doi.org/10.1016/j.ijpharm.2015.01.019
15. Gao S, Qiu Z, Ma Z, Yang Y (2017) Development of high efficiency infrared-heating-assisted micro-injection molding for fabricating micro-needle array. Int J Adv Manuf Technol 92:831–838. https://doi.org/10.1007/s00170-017-0169-5
16. Donnelly RF, Majithiya R, Singh TRR, Morrow DIJ, Garland MJ, Demir YK, Migalska K, Ryan E, Gillen D, Scott CJ, Woolfson AD (2011) Design, optimization and characterisation of polymeric microneedle arrays prepared by a novel laser-based micromoulding technique. Pharm Res 28:41–57. https://doi.org/10.1007/s11095-010-0169-8
17. Davis SP, Martanto W, Allen MG, Prausnitz MR (2005) Hollow metal microneedles for insulin delivery to diabetic rats. IEEE Trans Biomed Eng 52:909–915. https://doi.org/10.1109/TBME.2005.845240
18. Yung KL, Xu Y, Kang C, Liu H, Tam KF, Ko SM, Kwan FY, Lee TMH (2012) Sharp tipped plastic hollow microneedle array by microinjection moulding. J Micromech Microeng 22:015016. https://doi.org/10.1088/0960-1317/22/1/015016
19. Mishra R, Maiti TK, Bhattacharyya TK (2018) Design and scalable fabrication of hollow SU-8 microneedles for transdermal drug delivery. IEEE Sensors J 18:5635–5644. https://doi.org/10.1109/JSEN.2018.2840335
20. Nemani KV, Moodie KL, Brennick JB, Su A, Gimi B (2013) In vitro and in vivo evaluation of SU-8 biocompatibility. Mater Sci Eng C 33:4453–4459. https://doi.org/10.1016/j.msec.2013.07.001
21. Gao Z, Henthorn DB, Kim CS (2008) Enhanced wettability of an SU-8 photoresist through a photografting procedure for bioanalytical device applications. J Micromech Microeng 18. https://doi.org/10.1088/0960-1317/18/4/045013
22. Ma Y, Cao X, Feng X, Ma Y, Zou H (2007) Fabrication of superhydrophobic film from PMMA with intrinsic water contact angle below 90°. Polymer (Guildf) 48:7455–7460. https://doi.org/10.1016/j.polymer.2007.10.038
23. Huang H, Fu C (2007) Different fabrication methods of out-of-plane polymer hollow needle arrays and their variations. J Micromech Microeng 17:393–402. https://doi.org/10.1088/0960-1317/17/2/027
24. Wang PC, Paik SJ, Kim SH, Allen MG (2014) Hypodermic-needle-like hollow polymer microneedle array: fabrication and characterization. J Microelectromech Syst 23:991–998. https://doi.org/10.1109/JMEMS.2014.2307320
25. Wang PC, Paik SJ, Chen S, Rajaraman S, Kim SH, Allen MG (2013) Fabrication and characterization of polymer hollow microneedle array using UV lithography into micromolds. J Microelectromech Syst 22:1041–1053. https://doi.org/10.1109/JMEMS.2013.2262587
26. Le Thanh H, Ta BQ, The H Le et al (2015) Low-cost fabrication of hollow microneedle arrays using CNC machining and UV lithography. J Microelectromech Syst 24:1583–1593. https://doi.org/10.1109/JMEMS.2015.2424926
27. Mishra R, Maiti TK, Bhattacharyya TK (2018) Development of SU-8 hollow microneedles on a silicon substrate with microfluidic interconnects for transdermal drug delivery. J Micromech Microeng 28:105017. https://doi.org/10.1088/1361-6439/aad301
28. Gill HS, Denson DD, Burris BA, Prausnitz MR (2008) Effect of microneedle design on pain in human volunteers. Clin J Pain 24:585–594. https://doi.org/10.1097/AJP.0b013e31816778f9

29. Hwang KY, Park CS, Kim JH, Suh KY, Cho EC, Huh N (2010) The effects of adhesion energy on the fabrication of high-aspect-ratio SU-8 microstructures. J Micromech Microeng 20:117001. https://doi.org/10.1088/0960-1317/20/11/117001
30. Yang R (2006) Ultra-violet lithography of thick photoresist for the applications in biomems and micro optics. Louisiana State University
31. Rad ZF, Nordon RE, Anthony CJ et al (2017) High-fidelity replication of thermoplastic microneedles with open microfluidic channels. Microsystems Nanoeng 3:1–11. https://doi.org/10.1038/micronano.2017.34
32. Timoshenko S, Young DH (1962) Elements of strength of materials, 5th ed. Van Nostrand Reinhold
33. Waseem Ashraf M, Tayyaba S, Afzulpurkar N, Nisar A (2010) Fabrication and analysis of tapered tip silicon microneedles for MEMS based drug delivery system. Sensors and Transducers 122:158–172
34. Gupta J, Park SS, Bondy B, Felner EI, Prausnitz MR (2011) Infusion pressure and pain during microneedle injection into skin of human subjects. Biomaterials 32:6823–6831. https://doi.org/10.1016/j.biomaterials.2011.05.061